

Chaos to Synchronization and Dissipative Quantum Scarring in Open Coupled top-Dicke model in a Lossy Cavity

Debabrata Mondal, Sohan Pati, and S. Sinha

Indian Institute of Science Education and Research-Kolkata, Mohanpur, Nadia-741246, India

(Dated: May 25, 2026)

We present a variant of the Dicke model, termed as the open coupled-top Dicke model, which enables the exploration of rich non-equilibrium phenomena, particularly the fate of quantum scars in an open environment. This model can effectively be realized by coupling a two-species Bose–Josephson junction to a lossy cavity. Photon loss induces spontaneous synchronization via projection onto a dissipation-free subspace, along with transient chaos followed by restoration of synchronization and coherence. We identify two distinct scarring phenomena in the presence of dissipation. One remains protected, exhibiting persistent revivals, while the scar associated with the superradiant phase displays a dissipation-induced slow decay of the survival probability. Remarkably, for sufficiently small spin magnitude, the chaos-assisted macroscopic quantum tunneling is linked to the latter type of scarring. The results can be readily tested in ongoing cavity QED experiments and have broader applicability in other platforms.

Introduction: In recent years, chaos, ergodicity, and their deviations due to scarring phenomena in isolated quantum systems have attracted significant attention [1–8]. However, the influence of dissipation on these phenomena remains largely unexplored [9–19], despite its ubiquity. Although often viewed as detrimental, dissipation can be engineered to stabilize a wealth of non-equilibrium phenomena such as multistability [20–25], time crystals breaking time-translation symmetry [26–31], and synchronization among the degrees of freedom with phase and frequency locking [32–35]. Beyond preserving coherence via dissipation-free subspaces [36–44], dissipation itself can control information scrambling by taming chaos [19], enabling the emergence of order from chaos. Recent advances in ultracold atoms, cavity and circuit quantum electrodynamics [45–50] have enabled controllable open many-body platforms, leading to phases such as self-organized supersolid [51–53] and continuous time crystals [26–31].

Concurrently, many-body quantum scars (MBQS) [6–8, 54–69], first observed in cold-atom systems [54], reveal weak ergodicity breaking, with special eigenstates supporting athermal revival phenomena in an otherwise chaotic system. While single-particle scarring is linked to unstable classical orbits [70], the relation between MBQS and underlying instabilities is not straightforward due to the absence of an appropriate classical limit in generic interacting quantum systems [59–61, 63]. Importantly, the fate of quantum scars under dissipation raises a pertinent issue. Additionally, scarring in open systems remains elusive [71–75], as dissipation leads to mixed states, unlike isolated systems where scars are encoded in special eigenstates.

In this work, we investigate dissipation-induced emergent non-equilibrium phenomena and the fate of quantum scarring in an open environment using a system of two interacting spins coupled to a leaky cavity mode, which we refer to as the ‘open coupled-top-Dicke’

(OCTD) model, realizable in a cavity-coupled Josephson junction of two-component bosons. Dissipation arising from photon loss plays a central role in the emergence of synchronization between the two spins by projecting the dynamics onto a dissipation-free subspace, and in regulating chaos by rendering it a transient phenomenon with recovery of coherence. Notably, the model hosts two distinct classes of dissipative scarring, both originating from unstable steady states: one yields persistent, dissipation-protected oscillations, while the other, associated with an unstable superradiant phase, exhibits phase-space localization and slow diffusion. We further identify chaos-assisted collective tunneling between unstable superradiant branches for a small number of particles. The model and dynamical phenomena are presented schematically in Fig. 1.

The model and experimental realization: The coupled-top-Dicke model describes two anti-ferromagnetically interacting large spins of equal magnitude S coupled to a cavity mode of frequency ω_c ,

$$\hat{\mathcal{H}} = \omega_c \hat{a}^\dagger \hat{a} - J(\hat{S}_{1x} + \hat{S}_{2x}) + \frac{V}{S} \hat{S}_{1z} \hat{S}_{2z} + \frac{\lambda}{\sqrt{2S}} (\hat{S}_{1z} + \hat{S}_{2z})(\hat{a} + \hat{a}^\dagger), \quad (1)$$

where λ denotes the spin–cavity coupling. This model generalizes the Dicke model [76–84] and is realizable in a two-component bosonic Josephson junction (BJJ) coupled to a cavity (see the schematic of the setup in Fig. 1(a)). The BJJ is described by the Bose–Hubbard dimer [85–88],

$$\hat{\mathcal{H}}_{\text{BJJ}} = \sum_{i,\ell} \left[-\frac{J}{2} \hat{b}_{i,\ell}^\dagger \hat{b}_{i,\bar{\ell}} + \frac{V}{2N} \hat{n}_{i,\ell} \hat{n}_{i,\bar{\ell}} \right] \quad (2)$$

where $i = 1, 2$ labels species with equal population N , and $\ell = L, R$ denotes the two wells. In the Schwinger boson representation [89], this maps to two interacting spins of

magnitude $S = N/2$, forming the coupled-top model [66–68, 90]. The cavity coupling $\sum_i \frac{\lambda}{2\sqrt{N}}(\hat{a} + \hat{a}^\dagger)(\hat{n}_{iL} - \hat{n}_{iR})$ [91] then yields the Hamiltonian in Eq.(1) [92]. We set $\hbar = 1$ and measure energy (time) in units of $J(1/J)$. Notably, for $V = 0$, the model reduces to an experimentally realizable generalized Dicke model [25] of a binary atomic mixture; collective spin models are also relevant to trapped ions [93–98] and molecular magnets [99–101] with cavity or microwave control.

In the presence of photon loss with rate κ , the non-unitary evolution of the density matrix is described by the Lindblad master equation [102–104],

$$\dot{\hat{\rho}} = -i[\hat{\mathcal{H}}, \hat{\rho}] + \frac{\kappa}{2} (2\hat{a}\hat{\rho}\hat{a}^\dagger - \{\hat{a}^\dagger\hat{a}, \hat{\rho}\}). \quad (3)$$

In the limit $S \rightarrow \infty$, the collective variables $\alpha = \langle \hat{a} \rangle / \sqrt{S} = (x + ip) / \sqrt{2} = \sqrt{n} \exp(i\psi)$ with photon number $n = |\alpha|^2$, phase ψ and spins $\vec{s}_i = \langle \vec{S}_i \rangle / S$ can be treated classically [29, 105, 106] and the corresponding equations of motion (EOM), obtained from the master

equation (see Eq.(3)) are given by,

$$\dot{\alpha} = -\left(\frac{\kappa}{2} + i\omega_c\right)\alpha - i\frac{\lambda}{\sqrt{2}}(s_{1z} + s_{2z}) \quad (4a)$$

$$\dot{s}_{i+} = i\frac{\lambda}{\sqrt{2}}(\alpha + \alpha^*)s_{i+} + iVs_{i+}s_{i-} + iJs_{iz} \quad (4b)$$

$$\dot{s}_{iz} = \frac{iJ}{2}(s_{i+} - s_{i-}). \quad (4c)$$

Each spin can be represented as a vector $\vec{s}_i = \{\sin\theta_i \cos\phi_i, \sin\theta_i \sin\phi_i, \cos\theta_i\}$ over the unit Bloch sphere, which can also be described by the canonical conjugate variables ϕ_i and $z_i = \cos\theta_i$. In the context of BJJ, the population imbalance and the relative phase between the two wells are described by $\langle \hat{S}_{iz} \rangle / S \equiv z_i = (n_{iL} - n_{iR}) / N$ and ϕ_i , respectively.

We analyze the fixed points of the classical EOM and their stability [92, 107], which determine the dynamics and non-equilibrium phases. Quantum mechanically, physical quantities and the density matrix are computed using an ensemble of quantum trajectories within the stochastic wave-function formalism [108–110], with an initial choice of a product of coherent states.

Fixed points and phases: The fixed points $\mathbf{Q}^* = \{x^*, p^*, s_{ix}^*, s_{iy}^*, s_{iz}^*\}$ can be categorized into two classes and their configurations are schematically represented in Fig.1(c). First class describes to normal phases (NP) with vanishing photon number $n^* = 0$,

$$\text{NP}_1 : s_{ix}^* = 1, s_{iy}^* = s_{iz}^* = 0 \quad (5)$$

$$\text{NP}_2 : s_{ix}^* = J/V, s_{iy}^* = 0, s_{1z}^* = -s_{2z}^* = \pm \sqrt{1 - \left(\frac{J}{V}\right)^2}, \quad (6)$$

where NP₂ describes an antiferromagnetic spin configuration. The other class corresponds to the ferromagnetic superradiant phase (FSR₁), with non-vanishing photon number $n^* \neq 0$, in which both spins are aligned parallel to each other,

$$\text{FSR}_1 : z_1^* = z_2^* = \pm \sqrt{1 - \frac{J^2(\kappa^2 + 4\omega_c^2)^2}{[8\omega_c\lambda^2 - (\kappa^2 + 4\omega_c^2)V]^2}},$$

$$x^* = -\frac{8\omega_c\lambda}{(\kappa^2 + 4\omega_c^2)}z_1^*, p^* = \frac{\kappa q^*}{2\omega_c}, \phi_i^* = 0, \quad (7)$$

where positive and negative values of z_i^* correspond to two symmetry broken branches of FSR₁.

First, we discuss the isolated system, for which the ground state is described by the above-mentioned fixed points, in the respective parameter regimes. In the absence of the atom-photon coupling $\lambda = 0$, the system reduces to coupled top model, describing two interacting spins, for which NP₁ undergoes a bifurcation giving rise to two symmetry broken branches of NP₂ at $V_c = 1$, describing a quantum phase transition [66, 68], which persists even for moderate photon coupling λ . With increasing λ , both the normal phases NP₁, NP₂ undergo

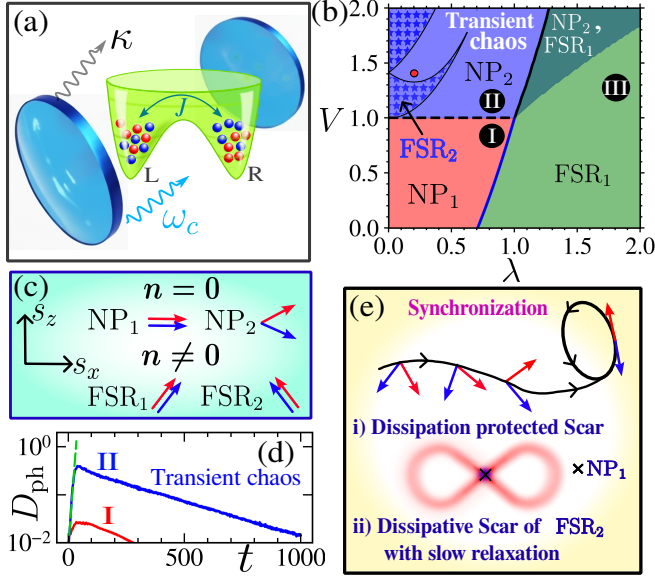


FIG. 1. (a) Schematic of a two-component Bose-Josephson junction (BJJ) inside a cavity with photon frequency ω_c and loss rate κ . (b) Phase diagram in λ - V plane for $\kappa = 0.3$, summarizing different dynamical regimes and fixed points. The stable regime of FSR₂ for the isolated case $\kappa = 0$ is marked by blue star-filled area. The scar of unstable FSR₂ in this work is shown at the coupling strength marked by red dot in (b). (c) Configuration of the fixed points schematically. (d) Dynamics of photonic decorrelator D_{ph} exhibiting transient chaos in region II of panel (b). (e) Pictorial representation of synchronization and dissipative scarring phenomena.

transitions to the superradiant FSR₁ phase. Notably, with dissipation, these fixed points are not full attractors, since the real parts of only two eigenvalues are negative while those of the others vanish, leading to the rapid decay of certain modes that underlie the emergent order.

In addition, another superradiant phase (with two branches corresponding to $\pm|z_i^*|$) arises as an excited state of the isolated system ($\kappa = 0$), denoted by

$$\text{FSR}_2 : \phi_1^* = \phi_2^* = \pi, \quad (8)$$

for which all variables coincide with FSR₁ except that the x -components of spins are oppositely aligned. For $\kappa \neq 0$, FSR₂ becomes unstable, yet it plays an important role in dissipative quantum scarring, as discussed later. The stability regimes of these fixed points for $\kappa \neq 0$, together with that of FSR₂ in the isolated case ($\kappa = 0$), are summarized in the phase diagram [Fig. 1(b)].

Importantly, the equations of motion are invariant under spin exchange ($S_1 \leftrightarrow S_2$), allowing categorization of dynamics into two classes. Introducing the new variables $s_{\pm a} = (s_{1a} \pm s_{2a})/2$ ($a = x, y, z$), the dynamical equations admit the following solutions,

$$\text{(I) anti-symmetric : } \{x = p = s_{x-} = s_{y+} = s_{z+} = 0\} \quad (9)$$

$$\text{(II) symmetric : } \{x, p \neq 0, s_{x-} = s_{y-} = s_{z-} = 0\}, \quad (10)$$

constraining the dynamics to reduced phase spaces. The class-I corresponds to an effective dissipation-free dynamics with vanishing photon number ($n = 0$) at the classical level, where the dynamics of remaining collective spin variables $\{s_{x+}, s_{y-}, s_{z-}\}$ reduce to the Hamiltonian dynamics of a Lipkin–Meshkov–Glick model [111]. The fixed points NP₁ and NP₂ belong to this class. We emphasize that a vanishing photon number alone is not sufficient to confine the system to the dissipation-free subspace. In addition, the spin configuration must satisfy the condition given by Eq.(9); otherwise, photons are generated dynamically during the evolution. Nevertheless, in general, the dynamics need not remain confined to these classes.

Although the photon field is coupled to the spins, in the normal phases (region I, II), the photon number vanishes at long times, effectively decoupling the spin (bosons) dynamics. Notably, the decay rate differs between these two phases, leading to distinct behavior discussed below.

Synchronization and transient chaos: In both regions I and II, the partially attracting fixed points NP₁ and NP₂, with vanishing photon number, influence the overall dynamics. Photon loss drives the cavity field to decay (shown in Fig.2(a,c)), effectively projecting the system onto a dissipation-free subspace described by anti-symmetric class I. This constrained dynamics enforces synchronization between the two spins (bosonic species), with $\phi_+ = (\phi_1 + \phi_2)/2 = 0$, $z_+ = (z_1 + z_2)/2 = 0$ independent of initial conditions. Quantum mechanically, this is reflected in the decay of $\langle \hat{n} \rangle$ and the vanishing of

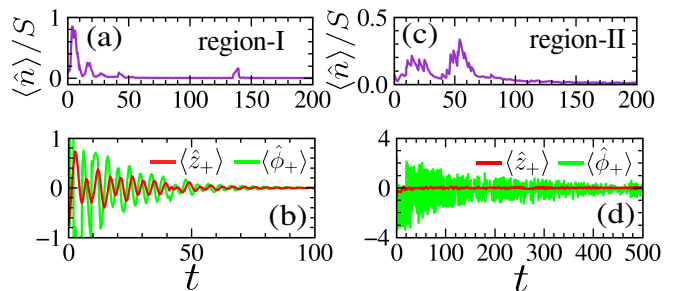


FIG. 2. *Synchronization and transient chaos:* Dynamics of (a,c) average photon number $\langle \hat{n} \rangle$, (b,d) relative phase $\langle \hat{\phi}_+ \rangle$ and $\langle \hat{z}_+ \rangle$ for single quantum trajectory corresponding to region-I (a,b) at $V = 0.5, \lambda = 0.5$, and region-II (c,d) at $V = 1.8, \lambda = 0.2$ of the phase diagram in Fig.1(b), respectively. Parameter chosen: $\kappa = 0.3, S = 6$ and sufficient number of Fock states to minimize truncation error. In this and the rest of the figures, we set $\hbar = 1$, measure energy (time) in units of $J(1/J)$ and choose $\omega_c = 1, J = 1$.

$\langle \hat{\phi}_+ \rangle$ and $\langle \hat{z}_+ \rangle$, even at the level of individual trajectories (see Fig.2(b,d)), along with suppressed fluctuations of these quantities. The key difference between the two regions lies in the timescale of synchronization.

In region I, where the dynamics is regular, the photon field decays rapidly, leading to fast synchronization. In contrast, in region II, the dynamics of the isolated system is generically chaotic, suppressing coherence and order. With photon loss, the spin (bosonic) sector decouples only at much longer timescales due to the competition between initial chaotic mixing and the partially attracting nature of NP₂, leading to long-lived transient chaos. Classically, the decorrelator dynamics of photon-field D_{ph} [112–114], exhibits exponential growth followed by decay (see Fig.1(d)), signaling the transient chaos. In region I, quantum trajectories starting from the same initial coherent state exhibit oscillatory dynamics in the remaining variables with the same frequency [92], akin to a boundary time crystal [115]. Nevertheless, transient chaos facilitates the emergence of order through synchronization and suppression of phase fluctuations of the bosons [85, 87, 92].

In region III, the fixed point FSR₁ is partially attracting with $\langle n \rangle \neq 0$, eventually giving rise to a self-organized non-equilibrium superradiant phase.

Next, we investigate the dissipative scarring phenomenon in region II, coexisting with transient chaos. The quantum–classical correspondence of this system enables exploration of true scars, typically linked to unstable fixed points and periodic orbits [6, 59–69]. We identify two types of scars, originating from unstable fixed points NP₁ and FSR₂, as discussed below.

(i) *Dissipation-protected scar of unstable NP₁:* As mentioned previously, the symmetry-unbroken normal phase NP₁ becomes unstable above the critical coupling V_c . Since scarred eigenstates are not well defined in

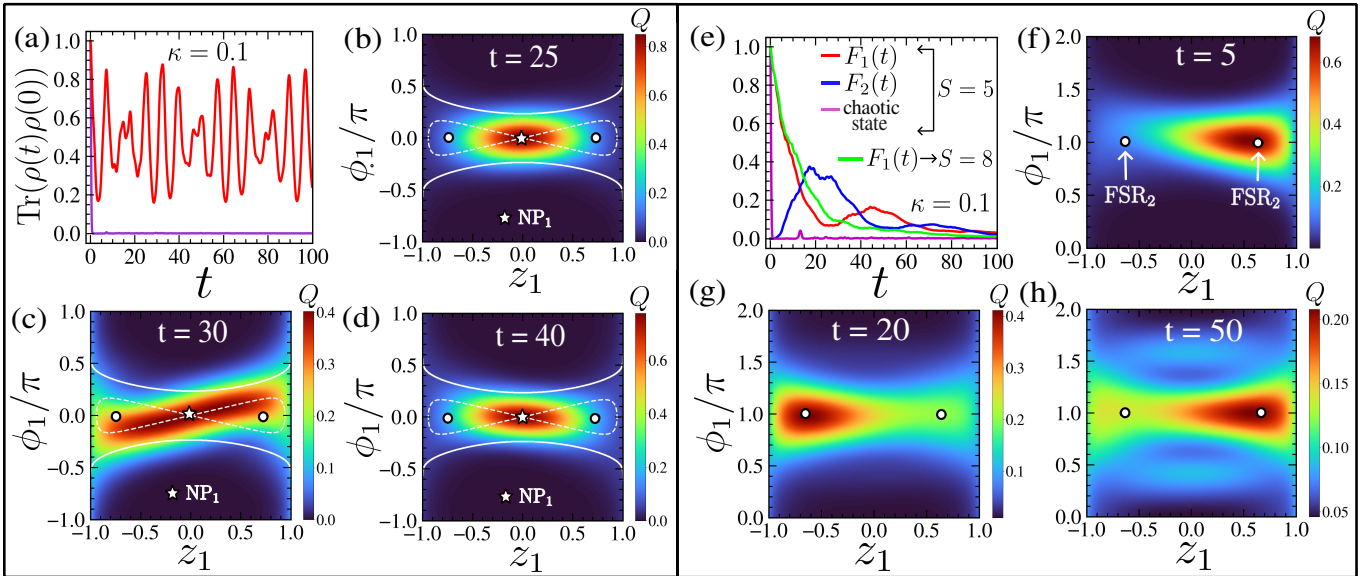


FIG. 3. *Quantum scarring phenomena of unstable NP₁*: (a) Dynamics of survival probability $\text{Tr}(\rho(t)\rho(0))$ and (b,c,d) Husimi distribution Q of reduced density matrix of one of the spins for three different times at $V = 1.5, \lambda = 0.5$. The purple and red lines correspond to the initial state representing a generic phase space point and unstable NP₁, respectively. *Quantum scarring phenomena of unstable FSR₂*: (e) Dynamics of the overlap corresponding to two branches of unstable FSR₂ $F_j(t)$ [see the main text], where (red, green) lines for $j = 1$ and blue line for $j = 2$. $F_1(t)$ corresponds to the survival probability. The green color line corresponds to $S = 8$. The purple line represents the survival probability starting from a generic phase space point. (f,g,h) Husimi distribution Q of reduced density matrix of one of the spins at three different times. Coupling strengths for panels (e-h) is $V = 1.4, \lambda = 0.2$ (see Fig.1(b)). Parameter chosen: $\kappa = 0.1, S = 5$ for all panels.

open systems, quantum scarring associated with unstable steady states in region II can only be probed dynamically, as dissipation yields mixed states. For this purpose, we evolve the system starting from the pure state $\hat{\rho}(0) = |\psi_c\rangle\langle\psi_c|$ constructed from the coherent state $|\psi_c\rangle$ representing the unstable fixed point (NP₁), and compute the survival probability $F(t) = \text{Tr}(\hat{\rho}(t)\hat{\rho}(0))$ over an ensemble of quantum trajectories. Interestingly, the survival probability $F(t)$ shows periodic oscillations without significant decay (Fig. 3(a)), exhibiting memory of the unstable NP₁ state even in the presence of dissipation. In contrast, $F(t)$ vanishes rapidly when the initial state corresponds to an arbitrary phase-space point in the chaotic region. Importantly, NP₁ is a saddle point on a homoclinic orbit enclosing two stable fixed points (NP₂). Under quantum evolution, an initially localized phase-space distribution at NP₁ spreads along this orbit and periodically accumulates near the saddle, as seen in the Husimi distribution (Fig. 3(b-d)), resulting in oscillations of the survival probability with negligible decay. Classically, as the spin dynamics is confined to a dissipation-free subspace, it results in a striking example of dissipation-protected quantum scarring [74].

(ii) *Dissipative scar of the unstable superradiant phase:*

As discussed earlier, for the isolated case in region II, another superradiant phase FSR₂ (with $\pm|z_i^*$ for two branches) exists as a stable excited state in the marked area of the phase diagram (Fig. 1(b)) and becomes un-

stable by appropriately changing the coupling strengths. In the presence of photon loss, to probe scarring phenomenon of unstable FSR₂, we evolve the initial density matrix $\hat{\rho}(0) = |\psi_{c1}\rangle\langle\psi_{c1}|$ starting from the coherent state $|\psi_{c1}\rangle$ representing one of the two branches of unstable FSR₂ phase and compute the survival probability $F_1(t)$ using an ensemble of quantum trajectories. The survival probability $F_1(t)$ exhibits a slow decay, as shown in Fig. 3(e), in contrast to oscillatory behavior in the isolated case [92]. Remarkably, this decay rate is significantly lower than that of a generic initial state in the chaotic regime, revealing the dissipative scarring effect of unstable FSR₂. Furthermore, from the time-evolved density matrix, we observe that for sufficiently large S , the semiclassical phase-space distribution remains localized around unstable FSR₂ for sufficiently long times with slow diffusion [92], indicating retention of memory of the unstable state even in the presence of dissipation. On the other hand, for sufficiently small spin magnitude, the survival probability $F_1(t)$ exhibits oscillatory behavior with overall decay. These oscillations originate from macroscopic quantum tunneling (MQT) [116–120] between two unstable branches of FSR₂. This is evident from the Husimi distributions at different times (Fig. 3(f-h)), showing accumulation of phase-space density around the two unstable branches in an alternating manner. This is further supplemented by computing the overlap $F_j(t) = \text{Tr}(\rho(t)|\psi_{cj}\rangle\langle\psi_{cj}|)$ between $\rho(t)$

and the two unstable branches $|\psi_{c_j}\rangle$ ($j = 1, 2$), which exhibit complementary behavior, as shown in Fig. 3(e). We emphasize that such MQT is suppressed in the stable regime of FSR₂ in an isolated system [92]. In contrast, for unstable FSR₂, mixing between the initially localized phase-space density and surrounding chaotic states facilitates tunneling between two unstable branches. This intriguing chaos-assisted MQT [121–124], linked to scarring, persists over a time window, beyond which phase-space diffusion sets in, leading to decay of $F_1(t)$.

Discussions: We present an experimentally accessible open coupled-top Dicke model exhibiting rich non-equilibrium phenomena and identify two distinct dissipative scarring mechanisms: one robust against dissipation with persistent revivals, and another linked to an unstable superradiant phase with dissipation-induced slow diffusion in phase space. Spontaneous synchronization through dynamical projection onto dissipation-free subspaces persists even in the presence of transient chaos, with restored coherence highlighting the constructive role of dissipation. Beyond these fundamental aspects, the model is also relevant to various platforms, enabling large-spin qudits, superradiant cat states for error correction, and controlled scrambling via transient chaos, with direct implications for quantum technologies and information processing.

Acknowledgment: We thank Lea F. Santos for valuable comments and fruitful discussions.

-
- [1] L. D’Alessio, Y. Kafri, A. Polkovnikov, and M. Rigol, *Advances in Physics* **65**, 239 (2016).
- [2] F. Borgonovi, F. M. Izrailev, L. F. Santos, and V. G. Zelevinsky, *Physics Reports* **626**, 1 (2016).
- [3] M. Rigol, V. Dunjko, and M. Olshanii, *Nature* **452**, 854 (2008).
- [4] J. M. Deutsch, *Reports on Progress in Physics* **81**, 082001 (2018).
- [5] O. Bohigas, M.-J. Giannoni, and C. Schmit, *Physical Review Letters* **52**, 1 (1984).
- [6] M. Serbyn, D. A. Abanin, and Z. Papić, *Nat. Phys.* **17**, 675 (2021).
- [7] A. Chandran, T. Iadecola, V. Khemani, and R. Moessner, *Annu. Rev. Condens. Matter Phys.* **14**, 443 (2023).
- [8] S. Moudgalya, B. A. Bernevig, and N. Regnault, *Rep. Prog. Phys.* **85**, 086501 (2022).
- [9] R. Grobe, F. Haake, and H.-J. Sommers, *Phys. Rev. Lett.* **61**, 1899 (1988).
- [10] G. G. Carlo, G. Benenti, and D. L. Shepelyansky, *Phys. Rev. Lett.* **95**, 164101 (2005).
- [11] G. Vivek, D. Mondal, S. Chakraborty, and S. Sinha, *Phys. Rev. Lett.* **134**, 113404 (2025).
- [12] F. Ferrari, L. Gravina, D. Eeltink, P. Scarlino, V. Savona, and F. Minganti, *Phys. Rev. Research* **7**, 013276 (2025).
- [13] D. Mondal, A. Kolovsky, and S. Sinha, *Phys. Rev. E* **111**, L052204 (2025).
- [14] L. Sá, P. Ribeiro, and T. Prosen, *Phys. Rev. X* **10**, 021019 (2020).
- [15] M. Prasad, H. K. Yadalam, C. Aron, and M. Kulkarni, *Phys. Rev. A* **105**, L050201 (2022).
- [16] D. Villaseñor, L. F. Santos, and P. Barberis-Blostein, *Phys. Rev. Lett.* **133**, 240404 (2024).
- [17] D. Villaseñor, H. Yan, M. Orel, and M. Robnik, *Phys. Rev. E* **112**, L042204 (2025).
- [18] D. Mondal, L. F. Santos, and S. Sinha, *Phys. Rev. Lett.* **136**, 040401 (2026).
- [19] D. Mondal, L. F. Santos, and S. Sinha, arXiv:2602.16817 (2026).
- [20] P. D. Drummond and D. F. Walls, *Phys. Rev. A* **23**, 2563 (1981).
- [21] G. Rempe, R. J. Thompson, R. J. Brecha, W. D. Lee, and H. J. Kimble, *Phys. Rev. Lett.* **67**, 1727 (1991).
- [22] H. Landa, M. Schiró, and G. Misguich, *Phys. Rev. Lett.* **124**, 043601 (2020).
- [23] L. Zhou, H. Pu, H. Y. Ling, and W. Zhang, *Phys. Rev. Lett.* **103**, 160403 (2009).
- [24] A. Ali, F. Saif, and H. Saito, *Phys. Rev. A* **105**, 063318 (2022).
- [25] F. Mivehvar, *Phys. Rev. Lett.* **132**, 073602 (2024).
- [26] H. Keßler, P. Kongkhambut, C. Georges, L. Mathey, J. G. Cosme, and A. Hemmerich, *Phys. Rev. Lett.* **127**, 043602 (2021).
- [27] P. Kongkhambut, J. Skulte, L. Mathey, J. G. Cosme, A. Hemmerich, and H. Keßler, *Science* **377**, 670 (2022).
- [28] X. Wu, Z. Wang, F. Yang, R. Gao, C. Liang, M. K. Tey, X. Li, T. Pohl, and L. You, *Nature Physics* **20**, 1389 (2024).
- [29] L. da Silva Souza, L. F. dos Prazeres, and F. Iemini, *Phys. Rev. Lett.* **130**, 180401 (2023).
- [30] S. Dutta, S. Zhang, and M. Haque, *Phys. Rev. Lett.* **134**, 050407 (2025).
- [31] P. Solanki, A. Cabot, M. Brunelli, F. Carollo, C. Bruder, and I. Lesanovsky, *Phys. Rev. A* **112**, L030601 (2025).
- [32] A. W. Laskar, P. Adhikary, S. Mondal, P. Katiyar, S. Vinjanampathy, and S. Ghosh, *Phys. Rev. Lett.* **125**, 013601 (2020).
- [33] Y. Li, Z. Xie, X. Yang, Y. Li, X. Zhao, X. Cheng, X. Peng, J. Li, E. Lutz, Y. Lin, and J. Du, *Sci. Adv.* **11**, eady5649 (2025).
- [34] A. Mari, A. Farace, N. Didier, V. Giovannetti, and R. Fazio, *Phys. Rev. Lett.* **111**, 103605 (2013).
- [35] A. Roulet and C. Bruder, *Phys. Rev. Lett.* **121**, 063601 (2018).
- [36] P. Zanardi and M. Rasetti, *Phys. Rev. Lett.* **79**, 3306 (1997).
- [37] D. A. Lidar, I. L. Chuang, and K. B. Whaley, *Phys. Rev. Lett.* **81**, 2594 (1998).
- [38] D. Bacon, J. Kempe, D. A. Lidar, and K. B. Whaley, *Phys. Rev. Lett.* **85**, 1758 (2000).
- [39] J. Kempe, D. Bacon, D. A. Lidar, and K. B. Whaley, *Phys. Rev. A* **63**, 042307 (2001).
- [40] P. G. Kwiat, A. J. Berglund, J. B. Altepeter, and A. G. White, *Science* **290**, 498 (2000).
- [41] J. B. Altepeter, P. G. Hadley, S. M. Wendelken, A. J. Berglund, and P. G. Kwiat, *Phys. Rev. Lett.* **92**, 147901 (2004).
- [42] M. Mohseni, J. S. Lundeen, K. J. Resch, and A. M. Steinberg, *Phys. Rev. Lett.* **91**, 187903 (2003).
- [43] Z. D. Walton, A. F. Abouraddy, A. V. Sergienko, B. E. A. Saleh, and M. C. Teich, *Phys. Rev. Lett.* **91**,

- 087901 (2003).
- [44] L.-X. Cen, Z. D. Wang, and S. J. Wang, *Phys. Rev. A* **74**, 032321 (2006).
- [45] F. Mivehvar, F. Piazza, T. Donner, and H. Ritsch, *Advances in Physics* **70**, 1 (2021).
- [46] I. Carusotto and C. Ciuti, *Rev. Mod. Phys.* **85**, 299 (2013).
- [47] S. Diehl, A. Tomadin, A. Micheli, R. Fazio, and P. Zoller, *Phys. Rev. Lett.* **105**, 015702 (2010).
- [48] H. Ritsch, P. Domokos, F. Brennecke, and T. Esslinger, *Rev. Mod. Phys.* **85**, 553 (2013).
- [49] A. Blais, A. L. Grimsmo, S. M. Girvin, and A. Wallraff, *Rev. Mod. Phys.* **93**, 025005 (2021).
- [50] A. A. Houck, H. E. Türeci, and J. Koch, *Nature Phys.* **8**, 292 (2012).
- [51] K. Baumann, C. Guerlin, F. Brennecke, and T. Esslinger, *Nature* **464**, 1301 (2010).
- [52] J. Klinder, H. Keßler, M. Wolke, L. Mathey, and A. Hemmerich, *Proceedings of the National Academy of Sciences of the United States of America* **112**, 3290 (2015).
- [53] J. Léonard, A. Morales, P. Zupancic, T. Esslinger, and T. Donner, *Nature* **543**, 87 (2017).
- [54] H. Bernien, S. Schwartz, A. Keesling, H. Levine, A. Omran, H. Pichler, S. Choi, A. S. Zibrov, M. Endres, M. Greiner, V. Vuletić, and M. D. Lukin, *Nature* **551**, 579 (2017).
- [55] S. Moudgalya, O. I. Motrunich, D. A. Huse, *et al.*, *Nature Physics* **18**, 1231 (2022).
- [56] C. J. Turner, A. A. Michailidis, D. A. Abanin, M. Serbyn, and Z. Papić, *Nat. Phys.* **14**, 745 (2018).
- [57] C. J. Turner, A. A. Michailidis, D. A. Abanin, M. Serbyn, and Z. Papić, *Phys. Rev. B* **98**, 155134 (2018).
- [58] C.-J. Lin and O. I. Motrunich, *Phys. Rev. Lett.* **122**, 173401 (2019).
- [59] W. W. Ho, S. Choi, H. Pichler, and M. D. Lukin, *Phys. Rev. Lett.* **122**, 040603 (2019).
- [60] A. A. Michailidis, C. J. Turner, Z. Papić, D. A. Abanin, and M. Serbyn, *Phys. Rev. X* **10**, 011055 (2020).
- [61] A. Pizzi, L.-H. Kwan, B. Evrard, C. B. Dag, and J. Knolle, *Nat. Commun.* **16**, 6722 (2025).
- [62] Q. Hummel, K. Richter, and P. Schlagheck, *Phys. Rev. Lett.* **130**, 250402 (2023).
- [63] B. Evrard, A. Pizzi, S. I. Mistakidis, and C. B. Dag, *Phys. Rev. B* **110**, 144302 (2024).
- [64] L. Gotta, S. Moudgalya, and L. Mazza, *Phys. Rev. Lett.* **131**, 190401 (2023).
- [65] S. Sinha and S. Sinha, *Phys. Rev. Lett.* **125**, 134101 (2020).
- [66] D. Mondal, S. Sinha, and S. Sinha, *Phys. Rev. E* **102**, 020101(R) (2020).
- [67] D. Mondal, S. Sinha, and S. Sinha, *Phys. Rev. E* **105**, 014130 (2022).
- [68] D. Mondal, S. Sinha, S. Ray, J. Kroha, and S. Sinha, *Phys. Rev. A* **106**, 043321 (2022).
- [69] D. Mondal, S. Sinha, and S. Sinha, *Phys. Rev. E* **104**, 024217 (2021).
- [70] E. J. Heller, *Phys. Rev. Lett.* **53**, 1515 (1984).
- [71] A. M. García-García, Z. Lu, L. Sá, and J. J. M. Verbaarschot, *Phys. Rev. E* **113**, 024116 (2026).
- [72] J.-L. Ma, Z. Guo, Y. Gao, Z. Papić, and L. Ying, *Phys. Rev. Lett.* **135**, 180401 (2025).
- [73] A. Teretenkov and O. Lychkovskiy, *Phys. Rev. B* **110**, L241105 (2024).
- [74] H.-R. Wang, D. Yuan, S.-Y. Zhang, Z. Wang, D.-L. Deng, and L.-M. Duan, *Phys. Rev. Lett.* **132**, 150401 (2024).
- [75] B. Buča, J. Tindall, and D. Jaksch, *Nature Communications* **10**, 1730 (2019).
- [76] R. H. Dicke, *Phys. Rev.* **93**, 99 (1954).
- [77] Z. Zhiqiang, C. H. Lee, R. Kumar, K. J. Arnold, S. J. Masson, A. S. Parkins, and M. D. Barrett, *Optica* **4**, 424 (2017).
- [78] M. P. Baden, K. J. Arnold, A. L. Grimsmo, S. Parkins, and M. D. Barrett, *Phys. Rev. Lett.* **113**, 020408 (2014).
- [79] F. Ferri, R. Rosa-Medina, F. Finger, N. Dogra, M. Soriante, O. Zilberberg, T. Donner, and T. Esslinger, *Phys. Rev. X* **11**, 041046 (2021).
- [80] C. Emary and T. Brandes, *Phys. Rev. Lett.* **90**, 044101 (2003).
- [81] A. Altland and F. Haake, *Phys. Rev. Lett.* **108**, 073601 (2012).
- [82] A. Baksic and C. Ciuti, *Phys. Rev. Lett.* **112**, 173601 (2014).
- [83] M. Soriante, T. Donner, R. Chitra, and O. Zilberberg, *Phys. Rev. Lett.* **120**, 183603 (2018).
- [84] K. C. Stitely, S. J. Masson, A. Giraldo, B. Krauskopf, and S. Parkins, *Phys. Rev. A* **102**, 063702 (2020).
- [85] R. Gati, B. Hemmerling, J. Fölling, M. Albiez, and M. K. Oberthaler, *Phys. Rev. Lett.* **96**, 130404 (2006).
- [86] T. Zibold, E. Nicklas, C. Gross, and M. K. Oberthaler, *Phys. Rev. Lett.* **105**, 204101 (2010).
- [87] R. Gati and M. K. Oberthaler, *J. Phys. B* **40**, R61 (2007).
- [88] D. Mondal, S. Sinha, S. Ray, J. Kroha, and S. Sinha, *Phys. Rev. A* **106**, 043321 (2022).
- [89] (), the Schwinger boson representation maps the bosonic operators to spin operators for each species of bosons as $\hat{S}_{ix} = \frac{1}{2}(\hat{a}_{iL}^\dagger \hat{a}_{iR} + \hat{a}_{iR}^\dagger \hat{a}_{iL})$ and $\hat{S}_{iz} = \frac{1}{2}(\hat{n}_{iL} - \hat{n}_{iR})$.
- [90] D. T. Robb and L. E. Reichl, *Phys. Rev. E* **57**, 2458 (1998).
- [91] R. Landig, L. Hruby, N. Dogra, M. Landini, R. Mottl, T. Donner, and T. Esslinger, *Nature* **532**, 476 (2016).
- [92] (), supplementary material provides the additional details on classical dynamics, dissipative phase transition, semiclassical dynamics of synchronization, chaos, coherence properties in oscillatory phase, and Liouvillian statistics.
- [93] C.-L. Hung, A. González-Tudela, J. I. Cirac, and H. J. Kimble, *Proc. Natl. Acad. Sci. U.S.A.* **113**, E4946 (2016).
- [94] R. Blatt and D. Wineland, *Nature* **453**, 1008 (2008).
- [95] A. Stute, B. Casabone, P. Schindler, T. Monz, P. O. Schmidt, B. Brandstätter, T. E. Northup, and R. Blatt, *Nature* **485**, 482 (2012).
- [96] R. Blatt and C. F. Roos, *Nat. Phys.* **8**, 277 (2012).
- [97] D. Porras and J. I. Cirac, *Phys. Rev. Lett.* **92**, 207901 (2004).
- [98] D. Leibfried, R. Blatt, C. Monroe, and D. Wineland, *Rev. Mod. Phys.* **75**, 281 (2003).
- [99] W. Wernsdorfer, N. Aliaga-Alcalde, D. N. Hendrickson, and G. Christou, *Nature* **416**, 406 (2002).
- [100] S. Hill, R. S. Edwards, N. Aliaga-Alcalde, and G. Christou, *Science* **302**, 1015 (2003).
- [101] J. Tejada, E. M. Chudnovsky, E. del Barco, J. M. Hernández, and T. P. Spiller, *Nanotechnology* **12**, 181 (2001).

- [102] V. Gorini, A. Kossakowski, and E. C. G. Sudarshan, *J. Math. Phys.* **17**, 821 (1976).
- [103] G. Lindblad, *Commun. Math. Phys.* **48**, 119 (1976).
- [104] H. P. Breuer and F. Petruccione, *The Theory of Open Quantum Systems* (Oxford University Press, Oxford, 2007).
- [105] F. Carollo and I. Lesanovsky, *Phys. Rev. Lett.* **126**, 230601 (2021).
- [106] C. J. Zhu, L. L. Ping, Y. P. Yang, and G. S. Agarwal, *Phys. Rev. Lett.* **124**, 073602 (2020).
- [107] S. H. Strogatz, *Nonlinear Dynamics and Chaos* (Westview Press, Boulder, CO, 2007).
- [108] A. J. Daley, *Advances in Physics* **63**, 77 (2014).
- [109] H. J. Carmichael, *An Open Systems Approach to Quantum Optics*, Lecture Notes in Physics, Vol. m18 (Springer-Verlag, Berlin, Heidelberg, 1993).
- [110] K. Mølmer, Y. Castin, and J. Dalibard, *Journal of the Optical Society of America B* **10**, 524 (1993).
- [111] H. J. Lipkin, N. Meshkov, and A. J. Glick, *Nuclear Physics* **62**, 188 (1965).
- [112] $\langle \cdot \rangle$, the decorrelator of photon field is defined as $D_{\text{ph}} = \frac{1}{\sqrt{(x^a - x^b)^2 + (p^a - p^b)^2}}$, where a, b correspond to two slightly perturbed initial configurations and the averaging is performed over an ensemble of randomly chosen initial conditions.
- [113] A. K. Chatterjee, A. Kundu, and M. Kulkarni, *Physical Review E* **102**, 052103 (2020).
- [114] S. Ruidas and S. Banerjee, *Physical Review Letters* **132**, 030402 (2024).
- [115] F. Iemini, A. Russomanno, J. Keeling, M. Schiró, M. Dalmonte, and R. Fazio, *Phys. Rev. Lett.* **121**, 035301 (2018).
- [116] A. J. Leggett, *Progress of Theoretical Physics Supplement* **69**, 80 (1980).
- [117] U. Weiss, *Quantum Dissipative Systems*, 4th ed., World Scientific Lecture Notes in Physics, Vol. 13 (World Scientific Publishing Company, Singapore, 2012).
- [118] A. O. Caldeira and A. J. Leggett, *Phys. Rev. Lett.* **46**, 211 (1981).
- [119] A. J. Leggett, S. Chakravarty, A. T. Dorsey, M. P. A. Fisher, A. Garg, and W. Zwerger, *Reviews of Modern Physics* **59**, 1 (1987).
- [120] M. H. Devoret, J. M. Martinis, and J. Clarke, *Physical Review Letters* **55**, 1908 (1985).
- [121] S. Tomsovic and D. Ullmo, *Phys. Rev. E* **50**, 145 (1994).
- [122] D. A. Steck, W. H. Oskay, and M. G. Raizen, *Science* **293**, 274 (2001).
- [123] M. Arnal, G. Chatelain, M. Martinez, N. Dupont, O. Giraud, D. Ullmo, B. Georgeot, G. Lemarié, J. Billy, and D. Guéry-Odelin, *Science Advances* **6**, eabc4886 (2020).
- [124] U. Satpathi, S. Ray, and A. Vardi, *Phys. Rev. E* **106**, L042204 (2022).

Supplemental Material: Chaos to Synchronization and Dissipative Quantum Scarring in Open Coupled top-Dicke model in a Lossy Cavity

Debabrata Mondal, Sohan Pati, and S. Sinha

Indian Institute of Science Education and Research-Kolkata, Mohanpur, Nadia-741246, India

This supplemental material provides additional figures and analyses that support the discussions in the main text.

DERIVATION OF OPEN COUPLED-TOP-DICKE MODEL AND CLASSICAL DYNAMICS

As discussed in the main text, the “open coupled-top Dicke” (OTCD) model, which describes two interacting large spins coupled to a cavity mode, can be realized using a cavity-coupled two-component Bosonic Josephson junction (BJJ). The corresponding system is described by a Bose–Hubbard dimer coupled to a cavity with the Hamiltonian [91]

$$\hat{\mathcal{H}} = \omega_c \hat{a}^\dagger \hat{a} - \frac{J}{2} \sum_{i=1,2} \left(\hat{a}_{iL}^\dagger \hat{a}_{iR} + \hat{a}_{iR}^\dagger \hat{a}_{iL} \right) + \frac{V}{N} (\hat{n}_{1L} \hat{n}_{2L} + \hat{n}_{1R} \hat{n}_{2R}) + \frac{\lambda}{2\sqrt{N}} \sum_{i=1,2} (\hat{a} + \hat{a}^\dagger) (\hat{n}_{iL} - \hat{n}_{iR}), \quad (\text{S11})$$

where the number of bosons for each species with index $i = 1, 2$ are equal and is given by $N = \hat{n}_{iL} + \hat{n}_{iR}$. Within the Schwinger boson representation, $\hat{S}_{i-} = \hat{a}_{iR}^\dagger \hat{a}_{iL}$, $\hat{S}_{iz} = (\hat{n}_{iL} - \hat{n}_{iR})/2$, this BJJ can be mapped to the system of two interacting large spins of equal magnitude $S = N/2$ (see Eq.1 of the main text), given by,

$$\hat{\mathcal{H}} = \omega_c \hat{a}^\dagger \hat{a} - J(\hat{S}_{1x} + \hat{S}_{2x}) + \frac{V}{S} \hat{S}_{1z} \hat{S}_{2z} + \frac{\lambda}{\sqrt{2S}} (\hat{S}_{1z} + \hat{S}_{2z}) (\hat{a} + \hat{a}^\dagger), \quad (\text{S12})$$

apart from the zero point energy term.

In this section, we discuss the classical dynamics and the various non-equilibrium phases of the open coupled-top-Dicke (OCTD) model in the presence of photon loss. The non-unitary evolution of the system’s density matrix $\hat{\rho}$ is governed by the Lindblad master equation, as given in Eq. (3) of the main text. The time evolution of the expectation value of any operator \hat{A} is obtained using the equation $\frac{d\langle \hat{A} \rangle}{dt} = \text{Tr}(\hat{A} \dot{\hat{\rho}})$. In the limit $S \rightarrow \infty$, the scaled operators

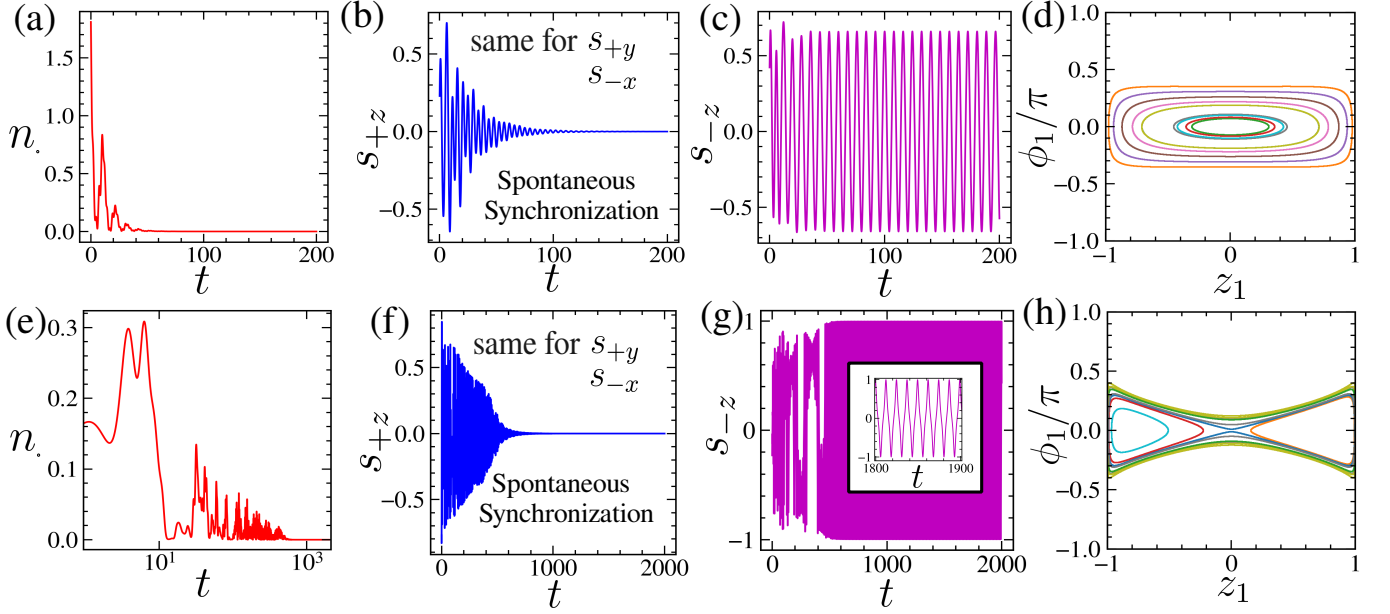


FIG. S4. Classical dynamics in region-I,II of the phase diagram in Fig.1(b) of the main text. The dynamics of (a,e) photon number n , collective spin variables (b,f) s_{+z} , (c,g) s_{-z} and (d,h) the phase-portrait in $z_1 - \phi_1$ corresponding to one of the spins for region-I,II at $(V = 0.5, \lambda = 0.5)$, $(V = 1.8, \lambda = 0.2)$, respectively. The timescale of synchronization is large for region-II compared to region-I due to the transient chaos. The inset of panel (g) clearly shows oscillatory behavior at long time. The phase portrait in the (d,h) plane is plotted over a long time interval after discarding the transient dynamics. Other parameters chosen for all the panels: $\omega_c = 1$, $J = 1$, $\kappa = 0.3$.

$\hat{a}/\sqrt{S} = (\hat{x} + i\hat{p})/\sqrt{2}$ and $\hat{s}_i = \hat{S}_i/S$ behave classically, since they satisfy the commutation relations $[\hat{x}_i, \hat{p}_i] = i/S$ and $[\hat{s}_{ia}, \hat{s}_{jb}] = \delta_{ij} \epsilon_{abc} \hat{s}_{ic}/S$, where $1/S$ plays the role of a reduced Planck constant. The classical equations of motion (EOM) for these collective variables can be derived from the master equation using the decoupling approximation $\langle \hat{A}\hat{B} \rangle \approx \langle \hat{A} \rangle \langle \hat{B} \rangle$ and are given by,

$$\dot{\alpha} = -\left(\frac{\kappa}{2} + i\omega_c\right)\alpha - i\frac{\lambda}{\sqrt{2}}(s_{1z} + s_{2z}) \quad (\text{S13a})$$

$$\dot{s}_{ix} = -\frac{\lambda}{\sqrt{2}}(\alpha + \alpha^*)s_{iy} - Vs_{iy}s_{iz}, \quad (\text{S13b})$$

$$\dot{s}_{iy} = \frac{\lambda}{\sqrt{2}}(\alpha + \alpha^*)s_{ix} + Vs_{ix}s_{iz} + Js_{iz}, \quad (\text{S13c})$$

$$\dot{s}_{iz} = -Js_{iy}, \quad (\text{S13d})$$

where the classical photon field is represented by $\alpha = \langle \hat{a} \rangle / \sqrt{S} = (x + ip) / \sqrt{2} = \sqrt{n} \exp(i\psi)$ with number $n = |\alpha|^2$ and phase ψ . The scaled spin vector can be written as $\vec{s}_i = (\sin \theta_i \cos \phi_i, \sin \theta_i \sin \phi_i, \cos \theta_i)$, where $s_{iz} = \cos \theta_i$ and ϕ_i are conjugate variables.

Fixed points and their stability: The steady states of the coupled-top-Dicke model are characterized by the fixed points $\mathbf{Q}^* = \{x^*, p^*, s_{ix}^*, s_{iy}^*, s_{iz}^*\}$ of the EOM [Eq.(S13)], obtained by setting $\dot{\mathbf{Q}} = 0$. The stability of each fixed point is determined by linearizing the EOM around \mathbf{Q}^* . A small fluctuation $\delta\mathbf{Q}$ from these fixed points evolves as $\delta\mathbf{Q}(t) = \delta\mathbf{Q}e^{\lambda t}$, where λ are the complex eigenvalues of the stability matrix [107].

A fixed point is a stable attractor if $\text{Re}(\lambda) < 0$ for all eigenvalues, in which case nearby trajectories converge to it. In contrast, for a Hamiltonian system (isolated case), the fixed points are center as $\text{Re}(\lambda) = 0$ for all eigenvalues, supporting periodic orbits around them. Unlike these two scenarios, in the present case, for all the fixed points (both normal (NP₁, NP₂) and superradiant (FSR₁) phases, see the main text), the real parts of only two eigenvalues are negative, while the remaining ones are zero. Consequently, the fluctuations of certain normal modes vanish, whereas the others persist as oscillations with frequency $\tilde{\omega} = \text{Im}(\lambda)$. This feature makes the fixed points partial attractors, where the dynamics is attracted towards them, but instead of converging to these fixed points, it eventually forms an orbit in a certain reduced phase space. Note that these oscillatory dynamics are different from limit cycles, as the orbits are not unique and the amplitude of oscillation depends on the initial fluctuation.

Anti-symmetric dynamical class and decoherence-free subspace: Next, we discuss the emergence of periodic orbits and spontaneous synchronization between the two spins [see the details in the main text]. As mentioned in the main text, the classical EOM (Eq.(S13)) of the OCTD model are invariant under the exchange of two spins ($S_1 \leftrightarrow S_2$), which plays a crucial role in the formation of coherent oscillatory phase. To understand the effect of this exchange symmetry on the dynamics, we rewrite the EOM in terms of the new classical variables $s_{\pm a} = (s_{1a} \pm s_{2a})/2$ ($a = x, y, z$), which are given by,

$$\dot{x} = \omega p - \frac{\kappa x}{2}, \quad (\text{S14a})$$

$$\dot{p} = -2\lambda s_{+z} - \omega x - \frac{\kappa p}{2}, \quad (\text{S14b})$$

$$\dot{s}_{\pm x} = -\lambda x s_{\pm y} - V s_{\pm y} s_{+z} + V s_{\mp y} s_{-z}, \quad (\text{S14c})$$

$$\dot{s}_{\pm y} = \lambda x s_{\pm x} + V s_{\pm x} s_{+z} - V s_{\mp x} s_{-z} + J s_{\pm z}, \quad (\text{S14d})$$

$$\dot{s}_{\pm z} = -J s_{\pm y}. \quad (\text{S14e})$$

It is evident from the above EOM (Eq.(S14)) that either of the following conditions

$$\text{(I) anti-symmetric : } \{x = p = s_{x-} = s_{y+} = s_{z+} = 0\} \quad (\text{S15})$$

$$\text{(II) symmetric : } \{x, p \neq 0, s_{x-} = s_{y-} = s_{z-} = 0\}, \quad (\text{S16})$$

can be satisfied, leading to the constraint dynamics in a reduced phase space. The fixed points and the corresponding dynamics can be classified into the above-mentioned categories, each satisfying its respective constraints. However, in general, the dynamics need not remain confined to these classes. The anti-symmetric dynamical class corresponds to the vanishing photon field, which determines the asymptotic dynamics of spins in the normal phase (parameter region I,II of the phase diagram in Fig.(1b) of the main text) as the photon number vanishes at long time due to dissipation (see Fig.S4(a,e)). Importantly, the constraint dynamics on the anti-symmetric dynamical class leads to the synchronization between the two spins $s_{x-} = 0, s_{y+} = 0, s_{z+} = 0$, irrespective of initial conditions, as depicted in Fig.S4(b,f). In the context of the Bosonic Josephson junction, the relative phase ϕ_i and the inter-well population imbalance z_i of the two species of bosons satisfy the constraints $\phi_+ = (\phi_1 + \phi_2)/2 = 0, z_+ = (z_1 + z_2)/2 = 0$, respectively. Moreover, the dynamics within the class-I reduces to an effective dissipation-free motion of spins since the photon field is zero, leading to a coherent oscillatory motion, as illustrated in Fig.S4(c,g). Consequently, the EOM of the other variables $\{s_{x+}, s_{y-}, s_{z-}\}$ reduces to an effective Hamiltonian dynamics governed by the Lipkin-Meshkov-Glick (LMG) model [111]. The long time spin dynamics in the plane of conjugate variables $\phi_i - z_i$ is regular periodic, as depicted in Fig.S4(d,h).

Transient chaos: In the isolated coupled-top-Dicke model ($\kappa = 0$), the onset of chaos occurs above the critical point $V > V_c = J$, which can be quantified using Lyapunov exponent [107]. However, when the photon loss is introduced, the vanishing of the photon field leads to synchronized dynamics between the two spins on a decoherence-free subspace, which causes the dynamics to follow that of the effective Hamiltonian of the integrable LMG model, suppressing chaos at long times. This behavior gives rise to the phenomenon of transient chaos, where chaotic dynamics persists only for intermediate times, while the asymptotic dynamics becomes regular. The transient chaos

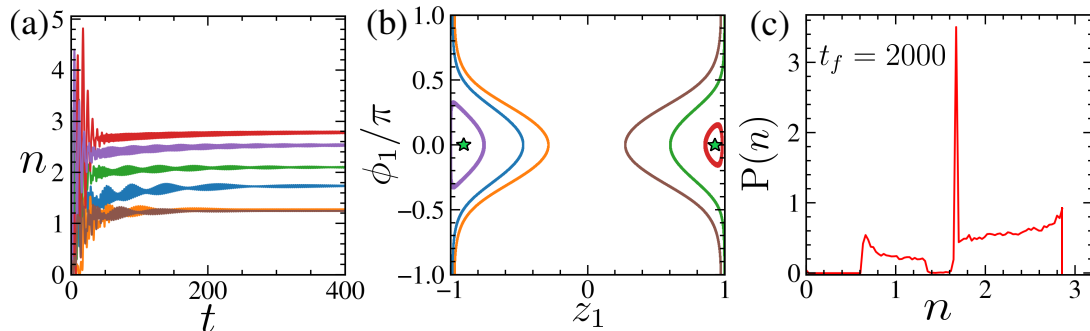


FIG. S5. Classical dynamics in region-III of the superradiant phase. (a) The dynamics of photon number n , (b) long time spin dynamics over $z_1 - \phi_1$ plane discarding the transient evolution, for different initial photon field and spin configurations. The same colors in panels (a,b) correspond to same initial conditions. (c) The stationary distribution values of photon number, starting from an ensemble of random initial conditions. The coupling strengths chosen: $\omega_c = 1, V = 0.5, \lambda = 1.3, \kappa = 0.3$.

can be characterized by the early-time exponential growth and the subsequent asymptotic decay of the photon-field decorrelator (see Fig. 1(d) of the main text), as well as by the time-dependent Lyapunov exponent.

Self-organized superradiant phase: Above a critical atom-photon coupling $\lambda_c(V)$, the normal phase undergoes a transition to a superradiant phase with nonzero photon number $n \neq 0$, as depicted in the phase diagram in Fig.1(b) of the main text. Interestingly, at long times, the photon number saturates to a steady value, which is however, not unique but differs on the initial conditions, as demonstrated in Fig.S5(a). The long-time steady-state photon number over the randomly chosen initial conditions attains a stationary distribution, which is shown in Fig.S5(b). Fascinatingly, the asymptotic photon distribution is quite non-uniform, giving rise to a self-organized superradiant phase. In the isolated case ($\kappa = 0$), the dynamics is chaotic in this regime. In contrast, with nonzero dissipation ($\kappa \neq 0$), as the photon number saturates to a steady value, the bosonic sector relaxes to certain emergent periodic orbits around the stable superradiant fixed point FSR₁ (see phase portrait in spin space in Fig.S5(c)), suppressing chaos at long times and giving rise to transient chaos.

SYNCHRONIZATION, COHERENT OSCILLATIONS AND PHASE FLUCTUATION

In the main text, we have shown the emergence of synchronization between the two spins (bosonic species) at the level of individual quantum trajectories as the photon loss projects the spin dynamics onto a decoherence-free subspace. In this section, we investigate the phenomenon of synchronization from the dynamics of the total density matrix $\hat{\rho}(t)$ and fluctuations of the relevant quantities, computed over an ensemble of quantum trajectories. The synchronization between two species of bosons can be investigated from the dynamics of symmetric population imbalance $\langle \hat{z}_+ \rangle = \langle (\hat{z}_1 + \hat{z}_2)/2 \rangle$ and associated relative phase $\langle \hat{\phi}_+ \rangle = \langle (\hat{\phi}_1 + \hat{\phi}_2)/2 \rangle$ between the two wells of BJJ and their respective fluctuations. To quantify the mean and fluctuations of relative phase, we adopt a quantum description of the phase operator based on a discrete phase representation [85–87]. The phase eigenstates are defined as

$$|\phi_m\rangle = \frac{1}{\sqrt{2S+1}} \sum_{n=-S}^S e^{in\phi_m} |n\rangle, \quad (\text{S17})$$

where $\phi_m = -\pi + \frac{2\pi m}{2S+1}$, with integer $m \in \{0, 1, \dots, 2S\}$ and $\phi_m \in [-\pi, \pi]$. Here, $|n\rangle$ denotes the eigenstates of the population-imbalance operator. The joint phase probability distribution associated with the reduced density matrix $\hat{\rho}_S$ of the combined two-species bosonic subsystem, obtained by tracing out the photonic degree of freedom from the total density matrix $\hat{\rho}(t)$, is given in the product phase basis by

$$p(\phi_{m1}, \phi_{m2}) = \langle \phi_{m1}, \phi_{m2} | \hat{\rho}_S | \phi_{m1}, \phi_{m2} \rangle, \quad \sum_{m1, m2} p(\phi_{m1}, \phi_{m2}) = 1.$$

The phase fluctuation $(\Delta\phi_+)^2$ is computed from this distribution as

$$(\Delta\phi_+)^2 = \sum_{m1, m2} \left[\left(\frac{\phi_{m1} + \phi_{m2}}{2} \right) - \langle \hat{\phi}_+ \rangle \right]^2 p(\phi_{m1}, \phi_{m2}), \quad (\text{S18})$$

where the mean collective phase is calculated as $\langle \hat{\phi}_+ \rangle = \sum_{m1, m2} \left(\frac{\phi_{m1} + \phi_{m2}}{2} \right) p(\phi_{m1}, \phi_{m2})$.

As evident from Fig.S6(a,b), in region I, the collective variables $\langle \hat{z}_+ \rangle, \langle \hat{\phi}_+ \rangle$, vanish at long times and their respective fluctuations $(\Delta z_+)^2, (\Delta\phi_+)^2$ also remain reasonably small, indicating synchronization between the two bosonic species (equivalently between two spins). On the other hand, in region-II, the fluctuations $(\Delta z_+)^2, (\Delta\phi_+)^2$ grow rapidly at early time due to the transient chaos; however, they decay slowly over time as the synchronization emerges eventually (see Fig.S6(c,d)).

Additionally, in region I, individual quantum trajectories starting from the same initial coherent state exhibit oscillatory dynamics in the remaining variables $\langle \hat{z}_- \rangle = \langle (\hat{z}_1 - \hat{z}_2)/2 \rangle, \langle \hat{\phi}_- \rangle = \langle (\hat{\phi}_1 - \hat{\phi}_2)/2 \rangle$ with the same frequency (see Fig.S7), resembling boundary time crystals [115]. However, there is a phase shift between different trajectories, which arises due to the coupling between spins (bosons) and photons at the early period of the dynamics.

Synchronization in the absence of spin-spin interaction: It is worth mentioning that in the absence of direct coupling between the two spins ($V = 0$), the model reduces to the generalized Dicke model [25] of a binary atomic mixture, which can readily be realized experimentally in cavity QED setups. Importantly, even in this regime, the synchronization occurs between the two spins spontaneously as evident from the vanishing of the quantities $\langle \hat{z}_+ \rangle, \langle \hat{\phi}_+ \rangle$ in Fig.S8.

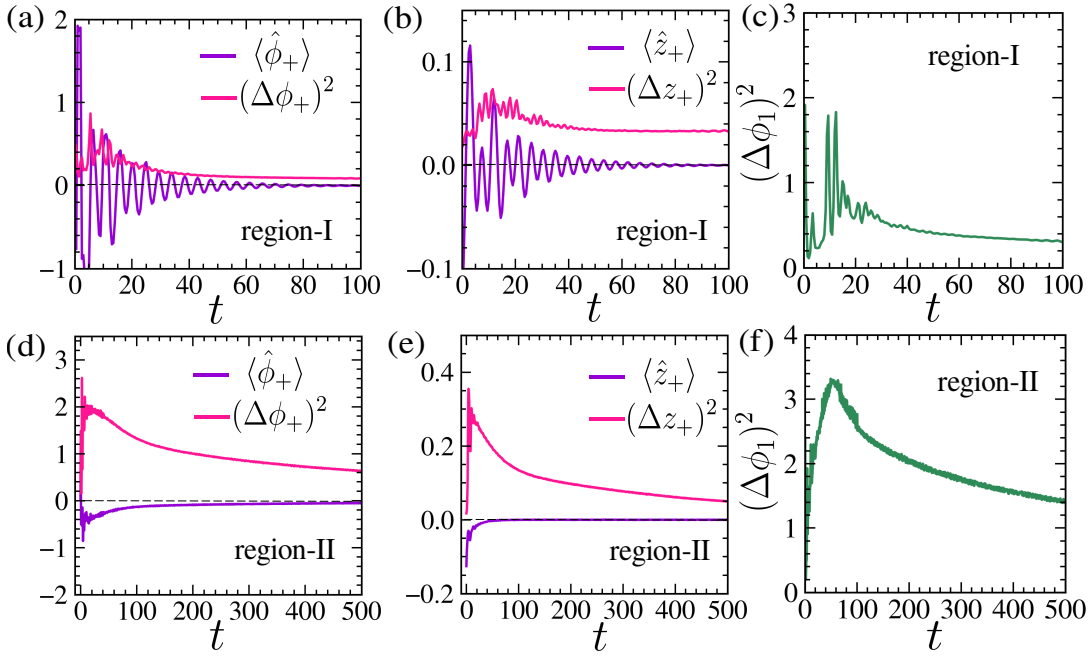


FIG. S6. Quantum signatures of synchronization and transient chaos. Dynamics of the symmetric collective variables formed from the two bosonic species, $\hat{z}_+ = (\hat{z}_1 + \hat{z}_2)/2$ and $\hat{\phi}_+ = (\hat{\phi}_1 + \hat{\phi}_2)/2$. Panels (a,d) show the dynamics of mean relative phase $\langle \hat{\phi}_+ \rangle$ and its fluctuation $(\Delta \phi_+)^2$; panels (b,e) show the mean symmetric population imbalance $\langle \hat{z}_+ \rangle$ and its fluctuation $(\Delta z_+)^2$; and panels (c,f) show the phase fluctuation of a single bosonic species, $(\Delta \phi_1)^2$, in regions I and II for parameters $(V = 0.5, \lambda = 0.5)$ and $(V = 1.8, \lambda = 0.2)$, respectively. Other parameters chosen: $\omega_c = 1, \kappa = 0.3, S = 6$.

Recovery of coherence and synchronization via transient chaos: In region II, the isolated system exhibits chaotic dynamics. However, in the presence of photon loss, the chaos is eventually suppressed due to dissipation-induced synchronization, resulting in transient chaotic behavior. The early-time mixing associated with this transient chaos is reflected in the rapid growth of fluctuations in the relative phase between the two wells of the BJJ for each bosonic species (see Fig. S6(d)). At longer times, these phase fluctuations decay again (see Fig. S6(d)), signaling the suppression of chaos. Importantly, the reduction of phase fluctuations also indicates a gradual restoration of coherence in the system.

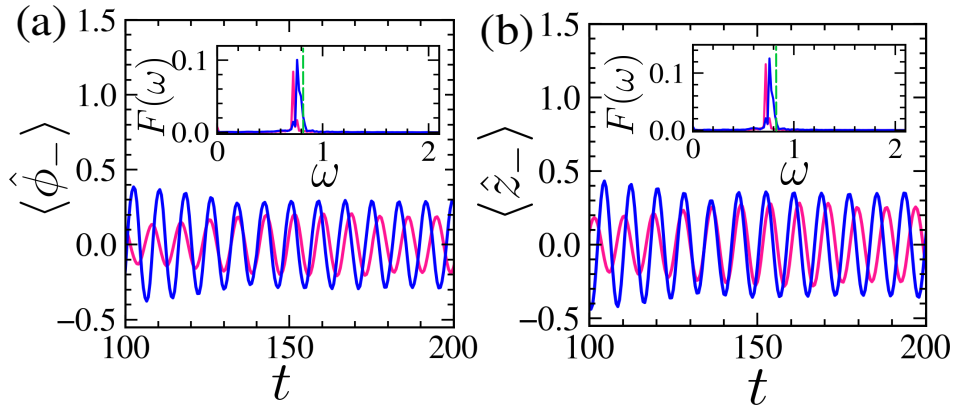


FIG. S7. Coherent oscillations in the regular dynamical region-I. The time evolution of collective (a) relative phase $\langle \hat{\phi}_- \rangle$ and (b) population imbalance $\langle \hat{z}_- \rangle$ for two different quantum trajectories starting from the same initial coherent state. The inset shows the Fourier spectrum of the dynamics of the respective variables. The parameters are chosen as $\omega_c = 1, \kappa = 0.3, V = 0.5, \lambda = 0.5, S = 6$.

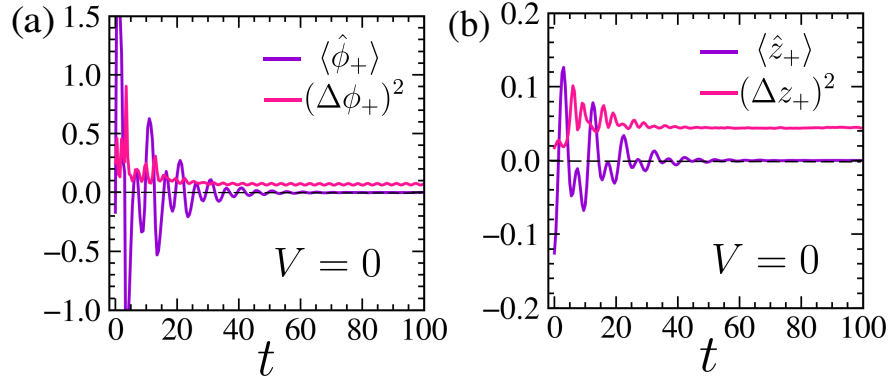


FIG. S8. Quantum signatures of synchronization from the dynamics of the symmetric collective variables: (a) relative phase $\langle \hat{\phi}_+ \rangle$ and its fluctuation $(\Delta \phi_+)^2$; (b) population imbalance $\langle \hat{z}_+ \rangle$ and its fluctuation $(\Delta z_+)^2$. Parameter chosen: $\omega_c = 1, V = 0.0, \lambda = 0.5, \kappa = 0.3, S = 6$.

SCARRING EFFECT OF UNSTABLE FSR₂

To this end, we discuss the quantum scars originated as a reminiscence of the unstable superradiant phase FSR₂ both in the isolated system and in the presence of dissipation. As discussed in the main text, the FSR₂ phase exists as a stable excited state in the isolated coupled-top-Dicke model within the parameter regime indicated in the phase diagram in Fig. 1(b) of the main text. First, we focus on the scarring phenomenon of FSR₂ in the isolated system ($\kappa = 0$). To analyze the classical phase space structure in the stable as well as in the unstable regime of FSR₂, we compute the Poincaré section at the fixed energy of FSR₂, using the surface of section defined by $p = 0$. The resulting dynamics is projected on the plane of conjugate variables $z_1 - \phi_1$ of one of the spin sectors. In the stable regime, regular islands form around the two branches of fixed points, embedded within a chaotic sea, as shown in the Poincaré section in Fig. S9(a). When FSR₂ becomes unstable, these regular islands vanish, and the fixed points are fully submerged in the chaotic region, as depicted in Fig. S10(a).

Signature of stable FSR₂ in isolated system: To investigate the quantum mechanical signature of this superradiant phase FSR₂, we consider an initial product coherent state $|\psi_{c1}\rangle$ representing one of the branch of FSR₂ and compute the survival probability $F_1(t) = |\langle \psi(t) | \psi_{c1} \rangle|^2$ from the time evolved state $|\psi(t)\rangle$. To visualize the evolution of the phase space density corresponding to the quantum state, we also obtain the Husimi distribution $Q(z_i, \phi_i) = \frac{1}{\pi} \langle z, \phi | \hat{\rho}_i | z, \phi \rangle$ of the reduced density matrix $\hat{\rho}_i = \text{Tr}_{\bar{i}} |\psi(t)\rangle \langle \psi(t)|$ of one of the spin sector. In the regime of stable FSR₂, the survival probability $F(t)$ remains close to unity and decays very slowly, retaining the memory of the initial state for a sufficiently long time, as depicted in Fig. S9(b). Consequently, the overlap $F_2(t) = |\langle \psi(t) | \psi_{c2} \rangle|^2$ of the time evolved state with the coherent state $|\psi_{c2}\rangle$ representing the other branch of FSR₂ remains vanishingly small. The Husimi distribution in Fig. S9(c,d) clearly displays the localized phase space density at one of the branches

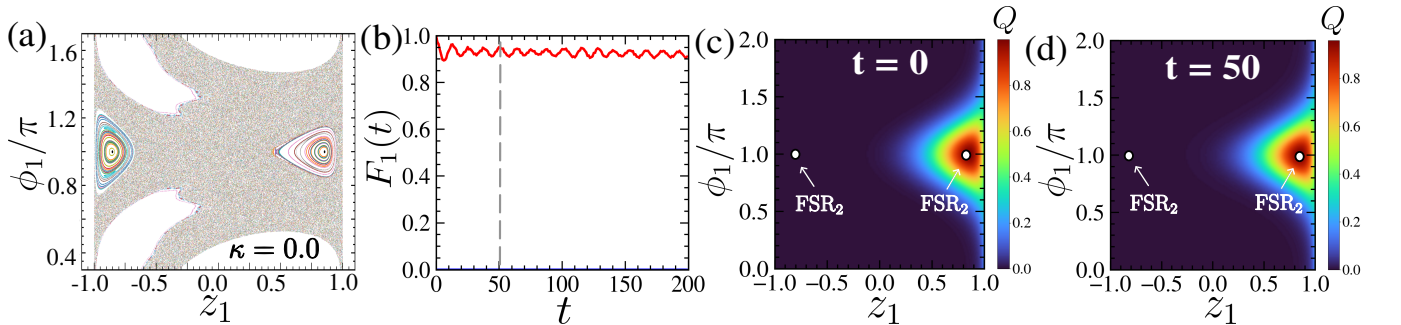


FIG. S9. Dynamical behavior around stable superradiant phase FSR₂ in isolated system. (a) The Poincaré section projected corresponding to one of the spin sectors. Regular island can be observed around the two branches of stable fixed points FSR₂. (b) Dynamics of the survival probability $F_1(t) = |\langle \psi(t) | \psi_{c1} \rangle|^2$ starting from the coherent state $|\psi_{c1}\rangle$ representing one of the branch of stable FSR₂. (c,d) Husimi distribution $Q(z_1, \phi_1)$ corresponding to one of the two spins in $z_1 - \phi_1$ plane at two different times $t = 0, 50$, for initial state $|\psi_{c1}\rangle$. The parameters are chosen as $\omega_c = 1, \kappa = 0.0, V = 2.0, \lambda = 0.2, S = 8$.

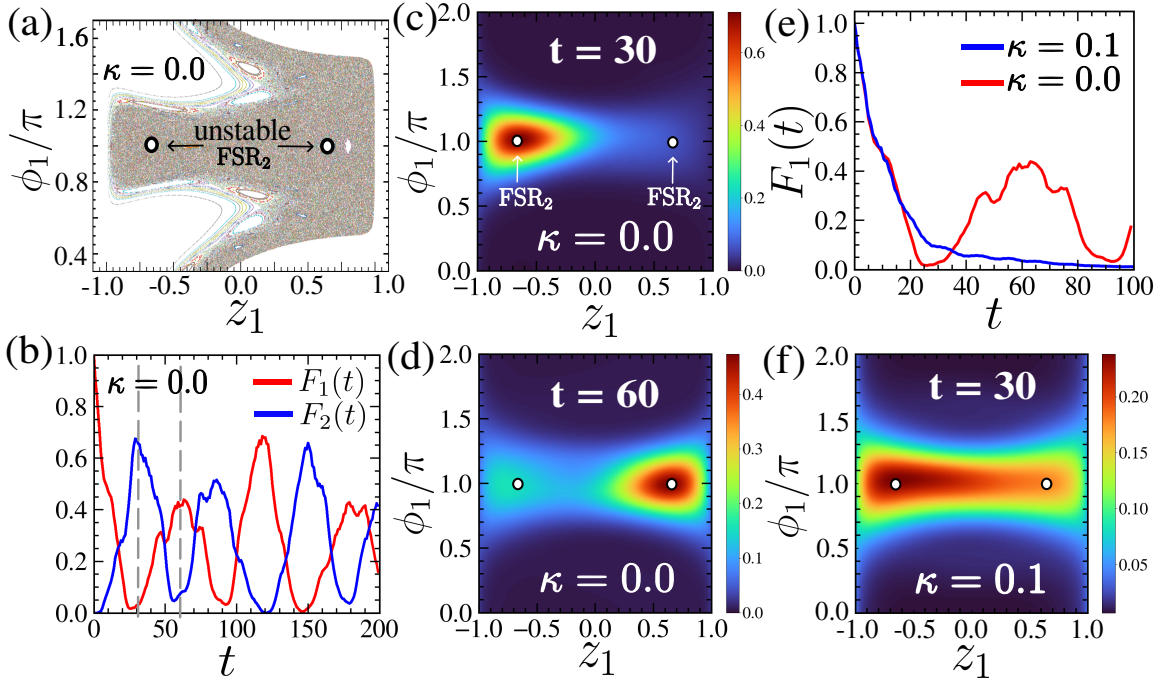


FIG. S10. Quantum scar of unstable FSR_2 both in isolated and dissipative systems. (a) The classical Poincaré section projected corresponding to one of the spin sector. (b) Dynamics of the overlaps $F_j(t) = |\langle \psi(t) | \psi_{cj} \rangle|^2$ of time evolved state $|\psi(t)\rangle$ with coherent states $|\psi_{cj}\rangle$ representing two branches of unstable FSR_2 in absence of photon loss $\kappa = 0$. (c,d) Husimi distribution $Q(z_1, \phi_1)$ corresponding to one of the two spins in $z_1 - \phi_1$ plane at two different times $t = 30, 60$ for $\kappa = 0$. (e) Comparison of survival probability $F_1(t) = \text{Tr}(\hat{\rho}(t) |\psi_{c1}\rangle \langle \psi_{c1}|)$ between isolated (red, $\kappa = 0$) and dissipative (blue, $\kappa = 0.1$) cases. Note that for isolated case, $\hat{\rho}(t) = |\psi(t)\rangle \langle \psi(t)|$. (f) Husimi distribution $Q(z_1, \phi_1)$ at time $t = 30$ in presence of photon loss $\kappa = 0.1$. In all panels, for quantum analysis, the initial state is the product coherent state $|\psi_{c1}\rangle$, representing one of the two branches of FSR_2 . Other parameters are chosen as $\omega_c = 1$, $V = 1.4$, $\lambda = 0.2$, $S = 8$.

of FSR_2 with a very slow diffusion.

Scar of unstable FSR_2 in isolated system: In contrast, when the FSR_2 is unstable, the survival probability $F_1(t)$ decays initially and exhibits revivals [Fig.S10(e)], revealing scarring phenomena. Whereas, for any generic initial states from the chaotic region, corresponding survival probability decays rapidly and vanishes. Interestingly, a collective tunneling between the two symmetry broken branches of unstable FSR_2 can be observed accompanied by this scarring effect. To show this phenomenon, we compute the overlap $F_2(t) = |\langle \psi(t) | \psi_{c2} \rangle|^2$ of the time evolved state with another branch of FSR_2 , which reveals a complementary behavior from that of $F_1(t)$, as depicted in Fig.S10(e). The collective oscillation of phase space density between the two branches of unstable FSR_2 is evident from the Husimi distribution at different times, which are shown in Fig.S10(c,d).

Scar of unstable FSR_2 in the presence of photon loss: To better understand the fate of scarring phenomenon in the presence of dissipation, we compute the survival probability $F_1(t) = \text{Tr}(\hat{\rho}(t)\hat{\rho}(0))$ for the dissipative system ($\kappa \neq 0$) by solving master equation using stochastic wave-function method for initial state $\hat{\rho}(0) = |\psi_{c1}\rangle \langle \psi_{c1}|$ and compare it with that of isolated ($\kappa = 0$) system. Note that, in an isolated system, the states are pure, for which the $F_1(t)$ reduces to the usual definition of survival probability mentioned earlier. As evident from Fig.S10(e), the initial decay of $F_1(t)$ is similar for both the dissipative ($\kappa \neq 0$) and isolated cases ($\kappa = 0$); however, at longer times, the non-dissipative case exhibits revival, whereas that of the dissipative system asymptotically vanishes over the same time scale. The Husimi distribution for $\kappa \neq 0$ exhibits significantly more diffusive behavior at long times compared to the $\kappa = 0$ case, as illustrated in Fig.S10(f).